WILEY | Hindawi

Research Article

Height of Mining-Induced Fractured Zones in Overlying Strata and Permeability of Rock with Nonpenetrative Fractures

Yu Liu [ID],[1] Qimeng Liu [ID],[2] Wenping Li,[3] and Youbiao Hu[2]

[1]*State Key Laboratory of Mining Response and Disaster Prevention and Control in Deep Coal Mines, Anhui University of Science and Technology, Huainan 232001, China*
[2]*School of Earth and Environment, Anhui University of Science and Technology, Huainan 232001, China*
[3]*School of Resources and Geosciences, China University of Mining and Technology, Xuzhou 221116, China*

Correspondence should be addressed to Qimeng Liu; qmliu@aust.edu.cn

Exploitation of shallow thick coal seams that are overlain by phreatic aquifers may cause loss of the water resource and destruction of the surface ecological environment. In order to explain the phenomenon that the actual leakage of phreatic water is greater than the predicted value, field investigation and analogue simulation were carried out, and the nonpenetrative fractured zone (NFZ) was proposed based on the original three zone theory. Further, a "vertical four-zone model" was established and the overlying strata was divided into a caved zone (CZ), through-going fractured zone (TFZ), NFZ, and continuous zone (COZ) from the bottom to the top. The characteristics of fractured rock within NFZ and the determination method of its height were studied. The results showed that the height of NFZ ranged from 11.55 to 21.20 m, which was approximately 0.17 times the combined height of the TFZ and the CZ. To reveal the mechanism of phreatic water leakage, the permeability of rock within NFZ was studied for their premining and postmining using an in situ water injection test and laboratory test. The results showed that the permeability of the rock in NFZ was increased by 7.52 to 48.37 times due to mining, and the magnitude of the increase was nonlinear from top to bottom. The increase of permeability of tested specimens was also related to the lithology. The results of the study are helpful to the prediction of the potential loss of phreatic water and the determination of the mining thickness.

1. Introduction

Study on mining induced fractures in overlying strata, and their influence on rock mass permeability is very important for underground engineering such as coal, oil, and metal mining and tunnel excavation [1–3]. Coal, accounting for approximately 94% of China's proven fossil energy reserves, is the most important energy source and the main industrial raw material to support China's development [4]. The deformation and failure of overlying strata during coal mining often lead to ground subsidence and water resources leakage, thereby threatening production safety and damaging even destroying ground construction and the ecogeological environment [5–7].

Many theories including "pressure arch," "cantilever beam," "articulated rock mass," "preformed fracture," "voussoir beam," "transferring rock beam," and "key stratum" have been put forward to explain the mining pressure and movement of overlying strata [8–11]. These theories have played an important role in understanding the overburden movement. In addition, the obvious zonation of the movement and failure of overlying strata due to longwall mining has been long recognized [12–14]. The "vertical three zone" model consisting of caved zone, fractured zone, and continuous zone of the strata movement and the distribution of mining induced fractures has been established [15, 16]. The fractured zone, also referred to as the vertical through-going fractured zone, and the caved zone are components of the fractured water-conducting fractured zone, which is the main pathway from the overlying aquifer into the gob [17–19]. However, the zonation is site specific. Other terms such as separation zone, loose alluvium zone, or downward fracture zone have been applied to different practical problems [3, 20–22].

The height of fractured zone in overlying strata is mainly influenced by rock mechanics parameters, lithology combination, stress, mining space size, and geological structure [23–25]. Methods for estimating the height mainly include material simulation, numerical simulation, and field measurement [26–28]. The results of field measurements are more representative of the actual situations; however, more effort is needed [29]. The failure heights of overlying strata have been observed and measured in hundreds of mining faces in different mining areas of eastern China. The empirical formula for calculating the heights of CZ and TFZ applicable to different mining conditions has been developed and included in the regulatory specifications and widely used [30]. However, there are few researches and studies in the mining areas of northwest China where thick coal seams are buried.

The study on permeability variation of fractured rock during coal mining was mainly based on numerical simulations and field tests [31]. Adhikary and Guo [29] carried out packer tests in an Australian coal mine to evaluate the permeability change of mining strata, and the results showed that the permeability of the surrounding rock was increased by more than 50 times, while the permeability of the roof rock over the goaf was increased by more than 1,000 times. Meng et al. [32] proposed a three-dimensional coupling model between stress and permeability and pointed out three stages of the permeability of coal seam roof during coal mining: decrease, increase, and gradual recovery. However, only few experimental works have been performed on the permeability of fractured rock after mining [33, 34].

The loss of sand layer water has a serious impact on coal mine production and longevity and the ecological environment in the arid and semiarid areas in NW China. The traditional three zone model takes the strata above the water conducting fractured zone as a whole, without considering its permeability change. However, the reduction of the water-resisting property of the rock in nonpenetrative fractured zone (NFZ) is the main reason for the loss of water resources. Using Stope #101 of Jinjitan Coal Mine as the case study, we designed and drilled nine boreholes from the ground surface down to the underground workings and established a "vertical four-zone model" with nonpenetrative fracture zone (NFZ) being proposed. The height of each zone was determined using hydrogeological borehole investigations and analogue simulation. Three types of rock, argillaceous sandstone, fine-grained sandstone, and siltstone within the NFZ, were studied for their premining and postmining water-resistant capacities using in situ water injection tests and laboratory permeability test. The results are of significance for designing the mining thickness of coal seams and determining the risk to loss of phreatic water resources, which are important theoretical bases for green mining.

2. Mining and Geological Conditions

Jinjitan Coal Mine is located in the northern part of Shaanxi province and to the south of the Mu Us desert at longitudes $109°42'32''\sim109°51'44''$ and latitudes $38°28'15''\sim38°35'59''$, encompassing an area of approximately $98.52\,km^2$ (Figure 1). Figure 2 shows the lithology overlying coal seam

2-2. Aquifers that overlie the coal seam include the sandstone confined aquifers of Yan'an and Zhiluo formations and the Quaternary phreatic aquifer of Sara Wusu formation. The water abundance of the confined aquifers is weak with the unit water inflow (q) ranging from 0.001 to 0.02 L/(s•m), while the water abundance of the phreatic aquifer is moderate with q ranging from 0.124 to 0.287 L/(s•m). In addition, the phreatic water is the most important water source for local residents and the ecosystem [35]. Because of lack of the N2 laterite, the fine-grained sandstone and argillaceous sandstone become the only relative aquiclude to prevent the leakage of phreatic water. The valuable phreatic water resources can suffer a serious leakage crisis during mining if the permeability of bedrock is increased.

The fully mechanized Stope #101 has elevations between +991.7 and +1010.4 m, whereas the corresponding surface elevations are between +1229.8 and +1263.7 m, respectively. The panel has a designed advance length of 4,548 m and a designed net face length of 300 m (Figure 1). Although the coalbed average thickness is 9.4 m, however, the mining thickness is only 5.5 m in order to avoid a large volume of phreatic water leakage and an ecological deterioration. The direct roof of coal seam 2-2 consists of dark gray argillaceous sandstone with a thickness of 3.03 m. The integrity of overlying strata is good with an average thickness of approximately 10 m. The roof is mainly composed of mudstone, argillaceous sandstone, siltstone, fine-grained sandstone, and medium-grained sandstone. The argillaceous sandstone, siltstone, and fine-grained sandstone are the main strata, accounting for 27.91%, 31.81%, and 29.52% of the total bedrock thickness, respectively.

3. Methodology

3.1. Hydrogeological Borehole Investigation. Hydrogeological borehole investigation is one of the most commonly used methods to study the development characteristics of fractures in overlying strata. It can also be used to evaluate the rock permeability with simple hydrogeological observation. In this study, nine boreholes were drilled at 2 months after mining when the gob had been stabilized. Figure 3 shows locations of the boreholes. Borehole JE5 was drilled in the nonmining area 150 m south of #2 return airway tunnel on Stope #101 to obtain the background data as a reference for other drilling data. Two profiles, A-A′ and B-B′, were arranged along the sloping direction of the working face. There were three boreholes (JE2, JE3, and JE4) on the A-A′ profile and three holes (JE6, JE7, and JE8) on the B-B′ profile. In addition, profile C-C′ was arranged along the advance direction on which there were four boreholes (JE1, JE3, JE8, and JE9). The buried depth of the coal seam in borehole JE1 through JE9 ranges from 258.58 to 267.28 m. Specifically, the buried depth of the coal seam is 262.70 m at JE1, 262.47 m at JE2, 260.55 m at JE3, 261.28 m at JE4, 263.20 m at JE5, 267.28 m at JE6, 262.10 m at JE7, 266.20 m at JE8, and 258.58 m at JE9. The hydrogeological investigations performed in these boreholes included drill-hole core analysis (DCA), drilling fluid loss measurement (DFLM), video camera observation (VCO), and field packer test (FPT).
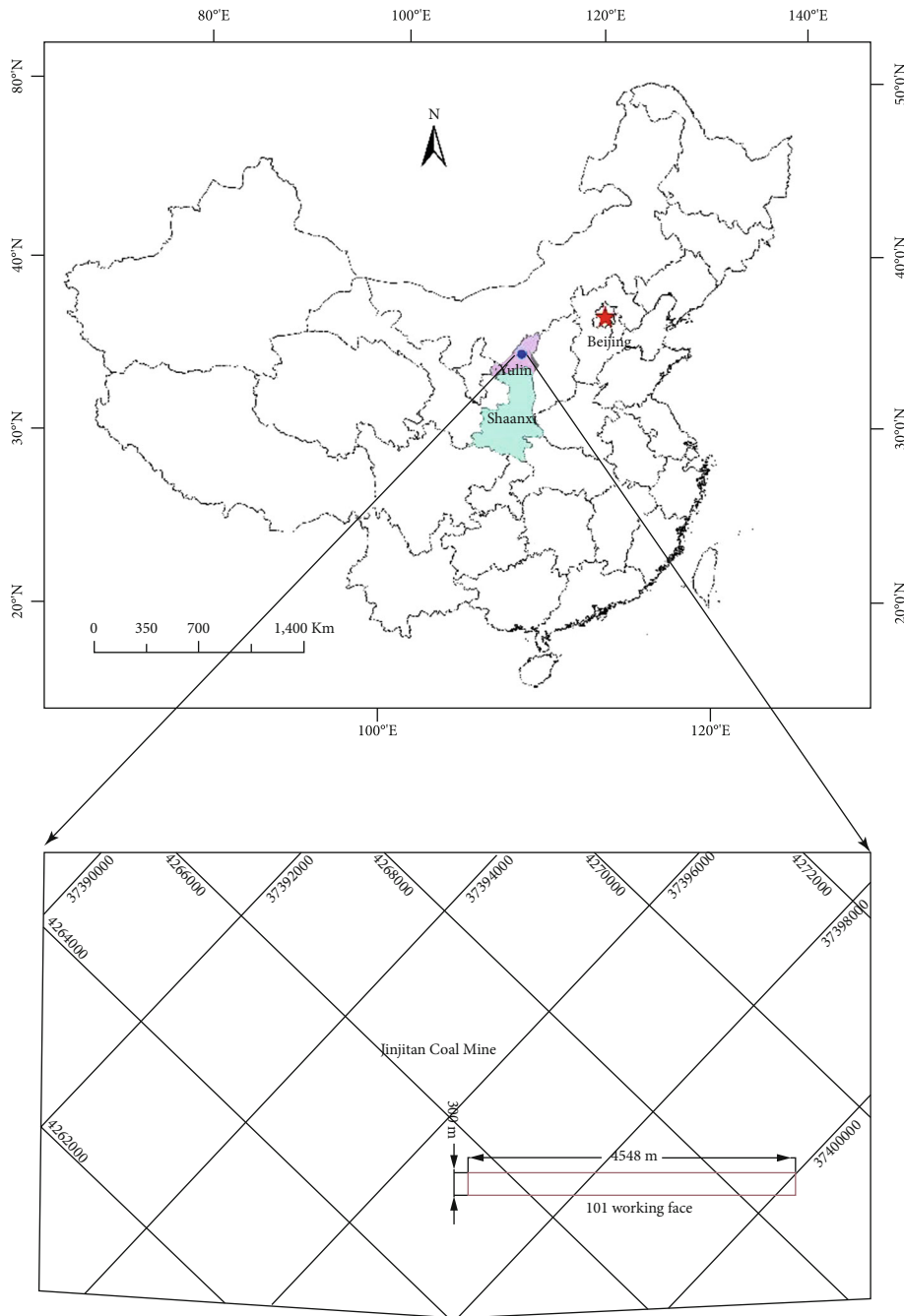
FIGURE 1: Location of Stope #101 and Jinjitan Coal Mine.

(i) Rock quality designation (RQD) can reflect the degree of rock integrity with higher values indicating better integrity. The appearance and density of fresh vertical or oblique fractures of the extracted cores were also visually observed. The RQD values of the normal rocks in the Jurassic Yan'an and Zhiluo formations of study area are generally greater than 60%. There are obvious differences of the rock permeability at different positions in overlying strata because of the differences in fracture shape, density, and width. The DCA method is particularly applicable

to determining the height of TFZ and CZ but not to determining the height of NFZ

(ii) The DFLM was conducted according to Standard MT/T865-2000. Drilling fluid consumption per unit time and the fluid depth were monitored dynamically. Where drilling fluid consumption started fluctuating and slowly increased with drilling depth and the fluid depth started to slightly decline or fluctuate, the position is regarded as the top interface of the NFZ. Where the fluid depth began to decline rapidly

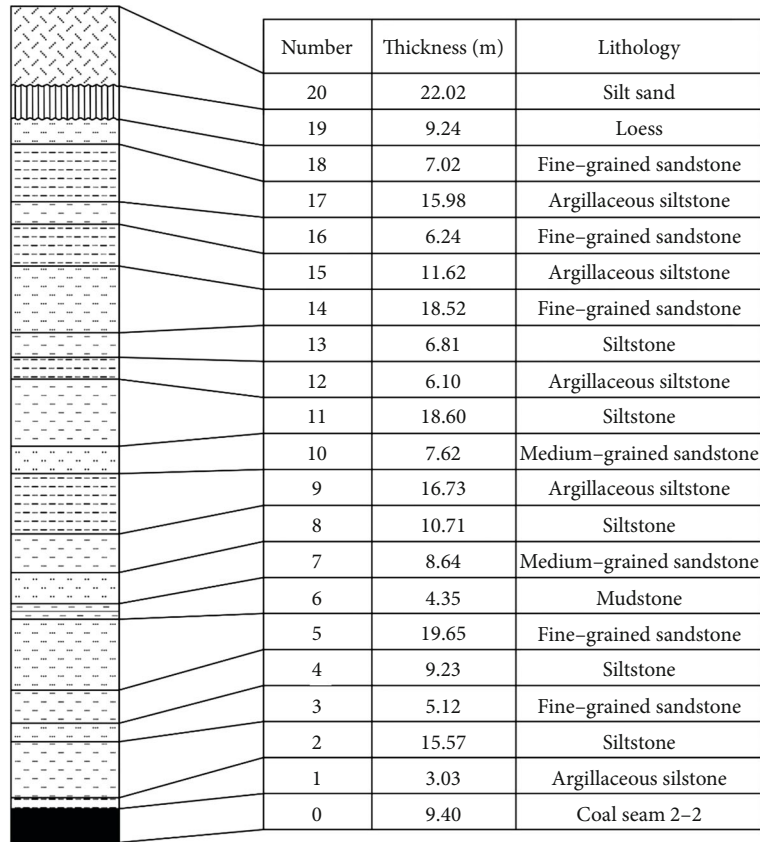| Number	Thickness (m)	Lithology
20	22.02	Silt sand
19	9.24	Loess
18	7.02	Fine–grained sandstone
17	15.98	Argillaceous siltstone
16	6.24	Fine–grained sandstone
15	11.62	Argillaceous siltstone
14	18.52	Fine–grained sandstone
13	6.81	Siltstone
12	6.10	Argillaceous siltstone
11	18.60	Siltstone
10	7.62	Medium–grained sandstone
9	16.73	Argillaceous siltstone
8	10.71	Siltstone
7	8.64	Medium–grained sandstone
6	4.35	Mudstone
5	19.65	Fine–grained sandstone
4	9.23	Siltstone
3	5.12	Fine–grained sandstone
2	15.57	Siltstone
1	3.03	Argillaceous silstone
0	9.40	Coal seam 2–2

FIGURE 2: Typical geological log profile of No. 101 panel overlying strata.
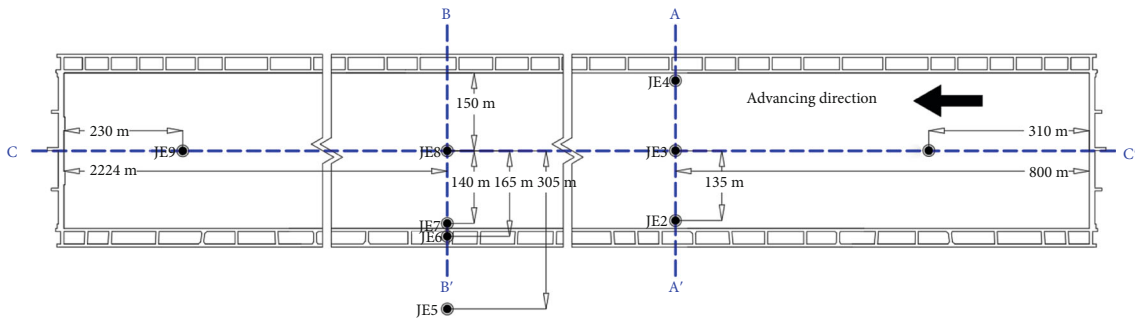

FIGURE 3: Boreholes layout at No. 101 working face.

and the fluid loss rate began to increase significantly with depth, the position is regarded as the top interface y of the TFZ

(iii) WDY-HW-60 video camera was used to visualize fractures in the borehole walls. It must be noted that the observations are possible only when the water in the borehole is clear and still. As a result, the image of the CZ cannot be obtained. Based on the images, the development characteristics of fractures in the inner walls of the borehole were analyzed, and the top boundary of TFZ and NFZ could be confirmed

(iv) The FPT was conducted by injecting water into the boreholes at 5 m intervals. The injection sequence was from bottom to top. Five pressures (0.3 MPa~0.6 MPa~1.0 MPa~0.6 MPa~0.3 MPa) were applied to each interval. Based on the amount of water injected, the rock permeability could be calculated. The position where the permeability increased by at least one order of magnitude and was above the TFZ was considered the top boundary of NFZ

3.2. Similar Material Physical Model. Similar material physical models have been used to study fracture development of overburden [9]. In this study, the dimensions of the physical model were 2,000 mm long by 220 mm wide by 1,300 mm high. These dimensions were designed to simulate mining

panel #101 at a ratio of 1 : 200. The kinematic and kinetic similarities to the actual mine system were also considered. The similarity constants for geometric time, bulk density, Poisson's ratio, stress, and intensity are listed in Table 1. The model was fully consolidated after 15 days of its construction. Then, the material representing the coal seam in the model was mined to simulate the mining processes. The movement and failure of overlying strata in the physical model were observed and measured to obtain the patterns of formation and height of the induced fractures. The type of materials and their quantities for building the physical model were based on test results of the mechanical parameters. Analogous materials of rocks in this experiment were admixtures of sand, gypsum, calcium carbonate, mica, and water with sand as the aggregate materials; gypsum and calcium carbonate as the bonding materials; and mica fragments as the layered materials. The model consisted of 22 layers. The simulated extraction parameters included 5.5 m coal seam, 320 m advancing length, and two 40 m coal pillars reserved on both sides of the model.

3.3. *Laboratory Permeability Test.* Permeability tests of the rock with different lithology were designed and carried out to investigate the permeability change in the NFZ in response to longwall mining. Nine core samples were taken from the NFZ in the boreholes and were cut into cylinders with 50 mm in diameter and 100 mm in length according to the suggestion by International Society for Rock Mechanics. The average dry densities of the fine-grained sandstones, siltstone, and argillaceous sandstone specimens are 2,395.21, 2,406.30, and 2,385.63 kg/m^3, respectively. The compressive strengths of the specimens were generally less than 20 MPa. According to the results of X-ray diffraction, the minerals in the sandstone material are feldspar, quartz, smectite, illite, calcite, and volcanic rock fragments. Table 2 lists the tested specimens and conditions. Because of low permeability of the test specimens, the transient flow method was adopted for permeability measurements.

The experiments for the sandstone specimens were carried out on a France-made TAW-1000 rock servo-controlled rock mechanics experimental system. Distilled water was chosen as the pore fluid. The test ambient temperature was kept at around 25 degrees to eliminate the effect of temperature on the experimental results.

4. Height of Fracture Zones in Overlying Strata

With the advance of panel, the overlying strata undergo a series of mechanical processes, such as movement, deformation, and fracture. According to the deformation and fracture characteristics of the overlying strata and its hydraulic conductivity, the overlying strata could be divided into several regions [12, 36]. For the purpose of evaluating leakage of phreatic water caused by mining of shallow thick coal seams, the results of field testing and similar material physical modeling suggest that the postmining overlying strata can be divided from bottom to top into four zones: caved zone (CZ), through-going fractured zone (TFZ), nonpenetrative fractured zone (NFZ), and continuous zone (COZ). The rock

stratum in the COZ has continuity and integrity and is the least affected by mining. The COZ may not exist under some conditions such as when the coal seam are shallow or the mining thickness is large. In addition, the height of COZ is mainly determined by the elevation difference between the top boundary of NFZ and the Surface. This article will discuss the three zones other than the COZ.

4.1. *Formation and Height of the CZ.* The CZ results from caving of the immediate roof strata into the mined-out area following coal extraction. The strata in the CZ lose not only the continuity of the formation but also the stratified bedding. The rock blocks in this zone are of different sizes and cluttered. The voids and thus connectivity are typically greater at the lower section of the zone. Because of the presence of collapsed rocks, one or more of the followings may occur when drilling into the CZ:

(i) There are frequently dropped drills

(ii) The drilling speed is unstable, and there are phenomena of being jammed and aggravated vibration of the drilling tools

(iii) The drilling process has obvious air suction phenomenon with audible whirring sound

The above indicators help determine the position of the top boundary of the CZ. The elevation difference between the top boundary and the coal seam floor is the height of the CZ. The observed phenomenon may not be the same for all boreholes. For example, in borehole JE2, the drill tool was stuck at a depth of 240.10 m with strong vibration, and at 241.22 m, there was a suction phenomenon, whereas in borehole JE9, a suction phenomenon was observed at 238.00 m and the drill dropped with 45 cm distance at a depth of 247.72 m. Therefore, the depths of 240.10 m and 238.00 m were considered the top boundaries of the CZ in boreholes JE2 and JE9, respectively. Table 3 presents the top boundary of the CZ at each borehole and the pertinent lines of evidence.

Figure 4 shows the drill-core photographs of borehole JE1. Figure 4(a) shows that the value of RQD is zero below 238.00 m. In comparison, the RQD value at the same position in the background borehole JE5 is approximately 80%. As a result, the depth of 238.00 m was considered the top boundary of the CZ in borehole JE1. The heights of the CZ in boreholes JE1, JE2, JE3, JE4, JE7, JE8, and JE9 were identified as 24.70, 23.47, 23.27, 23.08, 22.95, 24.50, and 23.78 m, respectively. In addition, the CZ was not observed in the JE6, which is 15 m away from the mining area.

The height of the CZ in Stope #101, as determined by the anomalies in the drilling process, ranges from 19.18 to 23.16 m with an average of 21.83 m. However, the height determined by RQD ranges from 22.27 to 24.70 m with an average of 23.54 m. As shown in Table 3, except for borehole JE3, the results determined by RQD are slightly larger than those determined from the drilling observations. In most cases, the RQD method has a higher resolution in determining the top boundary of the CZ. The larger value of the two methods was selected.

TABLE 1: Similarity condition of similar material simulation model to actual mine system.

Model size (mm^3)	Geometric	Time	Bulk density	Poisson ratio	Stress	Strength
2,000 × 220 × 1,300	1 : 200	1 : 14.14	1 : 1.5	1 : 1	1 : 300	1 : 300

TABLE 2: Tested sandstone specimens in this research.

Specimen	Length (mm)	Diameter (mm)	Mass (g)	Dry density (kg/m^3)	Clay content (%)	Position of the NFZ
F1	99.26	49.57	458.88	2395.51	28.3	Upper
F2	100.05	49.57	462.88	2397.31	31.2	Middle
F3	99.63	49.33	455.63	2392.82	29.6	Lower
S1	97.92	49.48	453.04	2406.11	32.5	Upper
S2	99.96	49.58	464.61	2407.46	34.9	Middle
S3	98.73	49.59	458.67	2405.32	32.7	Lower
A2	100.82	49.58	464.77	2387.75	44.9	Lower
A4	99.89	49.4	456.66	2385.21	40.1	Middle
A5	100.79	49.58	463.89	2383.94	39.0	Upper

TABLE 3: Top boundary depths and heights of the CZ in boreholes.

	Special phenomena in the drilling process			DCA			
Holes	Basis for determination	Top boundary depths the CZ (m)	Heights of the CZ (m)	Basis for determination	Top boundary depths the CZ (m)	Heights of the CZ (m)	Results (m)
JE1	At the depth of 240.00 m, drill dropped with 25 cm distance; at 241.40 m, suction phenomenon	240.00	22.70	Below 238.00 m, extremely broken core, RQD = 0	238.00	24.70	24.70
JE2	Drill tool was stuck at a depth 240.10 m with strong vibration; at 241.40 m, suction phenomenon	240.10	22.37	Below 239.00 m, broken core, RQD = 8.0%	239.00	23.47	23.47
JE3	During 237.00~238.00 m, drill dropped with 60 cm distance	237.00	23.55	Below 238.28 m, fragmental core, RQD = 8.4%	238.28	22.27	23.55
JE4	At 238.12 m, drill dropped with 30 cm distance; at 238.56 m, suction phenomenon	238.12	23.16	Below 237.20 m, fragmental core, RQD = 0	237.20	23.08	23.08
JE5	None	—	0	Integrity core, RQD = 66 ~ 85%	—	0	0
JE6	None	—	0	Integrity core, RQD = 63 ~ 75%	—	0	0
JE7	At 240.80 m, drill dropped with 15 cm distance; at 243.15 m, suction phenomenon	240.80	21.30	Below 239.15 m, broken core, RQD = 7.3%	239.15	22.95	22.95
JE8	At 247.02 m, drill dropped with 35 cm distance; at 239.00 m, suction phenomenon	247.02	19.18	Below 241.70 m, broken core, RQD = 10%	241.70	24.50	24.50
JE9	At 238.00 m, suction phenomenon; at 247.72 m, drill dropped with 15 cm distance, and drill tool was stuck	238.00	20.58	During 234.80~238.00 m, disorder bedding, RQD = 5.8%	234.80	23.78	23.78

FIGURE 4: Drill-core photographs of JE1 borehole: (a) RQD is zero of CZ; (b) first fresh vertical fracture and smaller RQD of TFZ; (c) initial high angle fracture and larger RQD of NFZ.

Therefore, determination of the height of the CZ is based on multiple lines of evidence. The final height of the CZ ranges from 22.95 to 24.70 m with an average of 23.72 m.

Figure 5 shows the magnitude and spatial distribution of the overburden failure zones in the analog model. The size of the grid is 10 cm × 10 cm, corresponding to the actual 20 m × 20 m. The immediate roof strata began to collapse after the simulated excavation advanced 40 m. When the working face advanced 120 m, the height of the CZ reached the maximum value of 23.89 m. Further mining did not increase the height. The maximum value and field measurements are very comparable, which verifies the validity and accuracy of the approach to determining the height of the CZ.

According to the above results and analyses, the height of the CZ is relatively stable at around 24 m, whether it is along the advancing or sloping direction. This average height is approximately 4.36 times of the mining thickness. In addition, the fact that no CZ was observed in borehole JE6 proves that the CZ develops only in the area above the working face.

4.2. Formation and Height of the TFZ. The TFZ is located above the CZ, where the rock retains the stratified bedding. The mining-induced fractures are well interconnected and provide the pathways for groundwater entering the gob. In many cases, the strata breakage gradually reduces upwards, resulting in the decrease of fracture network development thus the permeability in the upper section of the TFZ.

The presence of fresh vertical fractures in the rock strata and significantly lower RQD values than the background one at borehole JE5 are two indicators in determining the position of the top boundary of the TFZ. Figure 4(b) shows that the first fresh vertical fracture was identified at the depth of 162.15 m in borehole JE1 and the RQD value decreased significantly at the same location. More fractures were found with the increase of depth.

The method of determining the position of the TFZ based on the characteristics of fluid loss rate and fluid surface depth during drilling is used and considered to be accurate [32]. The measurement results of the background borehole JE5 show that the average rate of fluid loss was 0.054 L/s in loess and 0.069 L/s in bedrock. As shown in Figure 6, the loss rate did not increase with the depth during the drilling of borehole JE5, and the mud circulation was normal. The top boundary of the TFZ was determined by comparing the variation characteristics of the rock (loess) permeability in other boreholes with those at borehole JE5. For example, in borehole JE8, the rate of fluid loss did not increase until the

TFZ was encountered at a depth of 155.20 m where the fluid loss was increased to 1.23 L/s and the depth of fluid surface decreased gradually. As showed in Figure 7(c), the borehole video camera image shows vertical penetrating fractures at the depth of 156.90 m in borehole JE3, and no penetrating fracture was noted in the shallower positions.

Although the degree of fracture development of the overlying strata can be observed intuitively and the relative quantitative evaluation can be carried out from core logs, however, the following two defects should be taken into account:

(i) Due to the impact of the drill pipe, the rocks tend to be broken in the process of the core being raised, leading to an overestimate of the height

(ii) Due to the small range of drilling, there might be no obvious longitudinal fractures in the core even if the TFZ is encountered, resulting in an underestimate of the height

With the video camera images, the fractures in the hole-walls can be visualized. The overestimate error could be reduced to a great extent by comprehensive analysis of DCA and BVCO results. DFLM reflects the development of both macrofractures and microfractures in the borehole. The underestimate error could be reduced by comprehensive analysis of DCA and DFLM results. Such analyses lead to the following procedures in determining the top boundary of the TFZ:

Firstly, the results of the DCA were compared with the results of the BVCO, and the larger value (h_{th}^1) was selected.

Secondly, the results of DCA and DFLM were compared to choose a smaller value (h_{th}^2).

Finally, the arithmetic mean (h_{th}) of the above two results was taken as the top boundary of TFZ, as calculated in the following equations:

$$\begin{cases} h_{\text{th}} = \dfrac{h_{\text{th}}^1 + h_{\text{th}}^2}{2}, \\ h_{\text{th}}^1 = \max\left(h_{\text{th}}^d + h_{\text{th}}^b\right), \\ h_{\text{th}}^2 = \min\left(h_{\text{th}}^d + h_{\text{th}}^f\right). \end{cases} \quad (1)$$

The estimated positions of the top boundary and the height of the TFZ are presented in Table 4.
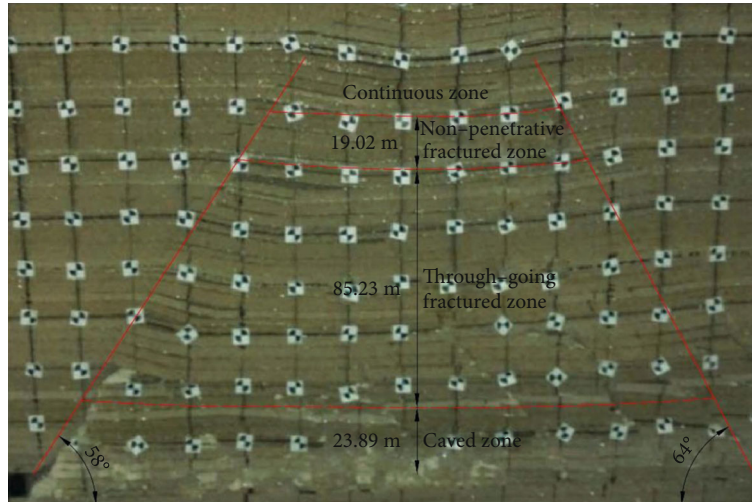
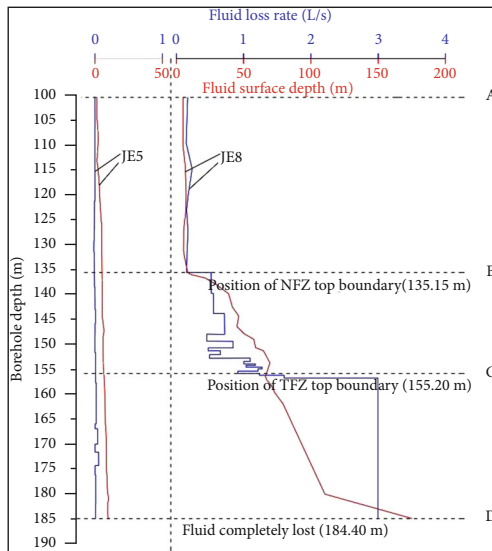FIGURE 5: The characteristics of overburden failure on the model.

FIGURE 6: The change of drilling fluid loss rate and fluid surface depth in JE8 borehole.

The results of the physical simulation showed that the height of the TFZ reached its maximum value of 85.23 m when the mining advanced 300 m. Unlike the CZ, the height of the TFZ varies with the spatial position. Figure 8 shows cross-sectional views of the induced height of the TFZ above Stope #101. The TFZ is arch-shaped along the sloping direction of the panel (Figure 8(a)), whereas the height gradually increases in the advance direction (Figure 8(b)). The height at the end of the mining panel is 1.22 times of the height at the beginning of the mining panel.

4.3. Formation and Height of the NFZ. The NFZ is located above the TFZ and deflects upward without apparent open fractures. Mining-induced fractures are present but small and isolated. Rock permeability tends to get smaller from bottom to top of the NFZ. The changes of rock permeability of TFZ are of great significance to design the mining height

and to prevent leakage of overlying phreatic sand aquifer. If the sand phreatic water overlie directly the NFZ or the NFZ is missing, the leakage can be significant.

Because the fractures are not fully penetrated and their lengths are small, there are no significant changes in the RQD values. For the same reasons, the video camera images failed to identify the position of the top boundary of the NFZ in the boreholes. The techniques used to determine the top boundary of the NFZ included DCA, VCO, DFLM, and packer testing.

Based on the DCA and VCO, in particular, where high angle fractures start to emerge (Figures 4(c) and 7(b)), the top boundaries of the NFZ were estimated in boreholes JE1, JE3, JE4, JE7, and JE9. Figure 6 shows the fluid loss rate and fluid surface depth in boreholes JE5 and JE8. The fluid loss rate fluctuated in the B-C segment between 135.15 m and 155.20 m. However, there is no dramatic increase, and the fluid surface depth slowly fell. Packer testing was conducted in all boreholes with the exception of boreholes JE5 and JE6 where no NFZ was developed.

The results of the top boundary and height of the NFZ are presented in Table 5. The results of DCA are similar to those of VCO, and the results of DFLM are similar to those from FPT. It appears that the estimated heights from DFLM and FPT are smaller than those from DCA and VCO. The reason is the results of DCA and VCO were based on field observations, while the results of DFLM and FPT were based on the hydrogeological properties of the rock. It is more accurate to determine the top boundary of the NFZ from the changes of hydrogeological properties. The minimum value of the results from the four methods was used as the conservative estimate of the top boundary of NFZ. The results of analogue simulation show that there are independent small fractures in the range of 19.02 m above TFZ.

The estimated height of the NFZ ranges from 11.55 to 21.20 m (Table 5). The height of the NFZ is approximately 0.17 times the combined height of the TFZ and the CZ, and this ratio is also confirmed by the analogue simulation results.
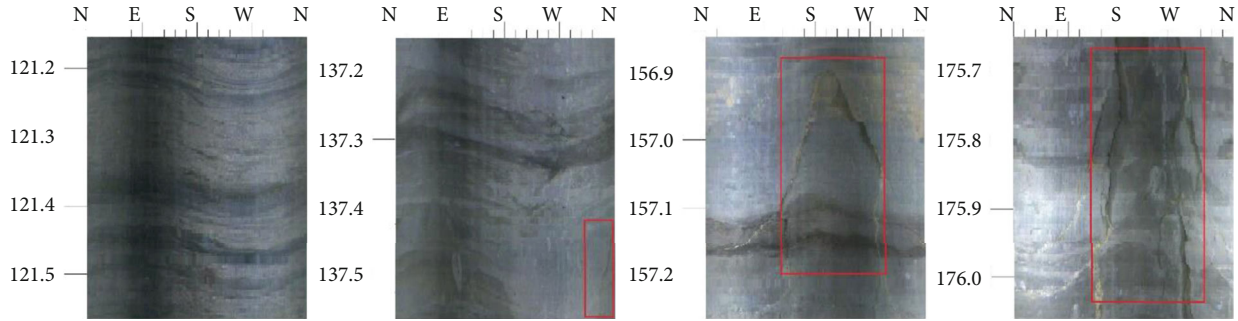
FIGURE 7: Video camera images of JE3 borehole: (a) no fracture; (b) initial high angle no-though fracture; (c) first fresh penetrative vertical fracture; and (d) TFZ.

TABLE 4: Top boundary depths and heights of the TFZ in boreholes.

Boreholes	Top boundary depths of the TFZ (m)				Heights of the TFZ (m)			
	DCA	DFLM	VCO	Final results	DCA	DFLM	VCO	Final results
JE1	162.15	161.7	162.15	161.93	75.85	76.3	75.85	76.07
JE2	199.43	199.47	199.55	199.51	39.57	39.53	39.45	39.49
JE3	155.98	155.55	156.9	156.23	81.02	81.45	80.1	80.77
JE4	191.47	195.28	196.78	194.13	46.73	42.92	41.42	44.07
JE5	0	0	0	0	0	0	0	0
JE6	0	0	0	0	0	0	0	0
JE7	172.2	172.1	172.2	172.15	46.95	47.05	46.95	47
JE8	155	155.2	155.3	155.15	86.7	86.5	86.4	86.55
JE9	145.83	145.58	145.63	141.71	88.97	89.22	89.17	93.09

5. Permeability of Rock within Nonpenetrating Fracture

The results of FPT in the background borehole JE5 show that the estimated permeability values of the argillaceous sandstone, siltstone, and fine-grained sandstone are 7.9×10^{-6} cm/s, 6.7×10^{-6} cm/s, and 5.5×10^{-6} cm/s, respectively. According to the standard for permeability classification of rock mass, the premining rocks are not conducive to water flow.

The transient-pulse permeability tests were used determine the permeability of postmining rock core samples collected in the boreholes. It took approximately one hour to reach a balance of the upstream pressure and downstream pressure, but after 0.1 h permeating, an obvious change trend occurred. If a transient pulse test lasts too long, the creep deformation of specimen under high compression stress occurs, which could cause a larger error of transient pulse tests. As a result, a proper test time ranging from 10 to 20 min was selected to short the total test time of a compression test.

Figure 9 shows the permeability test results. In this figure, P0 represents the position not affected by mining; P1, P2, and P3 represent the upper, middle, and lower sections of NFZ, respectively. Figure 9(a) shows that the permeability of the argillaceous sandstone was significantly increased after mining. The degree of change is closely correlated with the locations of the argillaceous sandstone. The permeability coefficients of the upper, middle, and lower sections of the argillaceous sandstone of NFZ increased from 5.52×10^{-6} cm/s to 4.2×10^{-5} cm/s, 1.11×10^{-4} cm/s, and 1.88×10^{-4} cm/s, an increase of 7.53, 20.04, and 34.13 times, respectively. The mining operations caused increases in permeability of rocks within the NFZ by 7.52 to 48.37 times. The magnitude of the increase in permeability decreases from bottom to top (Figure 9). Figures 9(b) and 9(c) show the degree of change in the permeability of siltstones and fine-grained sandstones. Similar to argillaceous sandstones, the permeability changes were closely correlated with their locations. The permeability coefficient of the siltstone in the upper, middle and lower parts of the NFZ increased to 6.33×10^{-5} cm/s, 1.32×10^{-4} cm/s, and 2.82×10^{-4} cm/s from the original 6.73×10^{-6} cm/s, increasing by 9.40, 19.58, and 41.93 times, respectively. The permeability coefficient of the fine-grained sandstone located in the upper, middle, and lower parts of the NFZ increased from 7.92×10^{-6} cm/s in a natural state to 8.69×10^{-5} cm/s, 1.67×10^{-4} cm/s, and 3.83×10^{-4} cm/s, respectively, increasing by 10.97, 21.05, and 48.37 times. Affected by mining, the rock permeability was changed significantly, and the maximum increase of the permeability coefficient could reach two orders of magnitude. Under the influence of mining, the permeability of fine-grained sandstone is the largest, followed by siltstone, and argillaceous sandstone is the smallest.
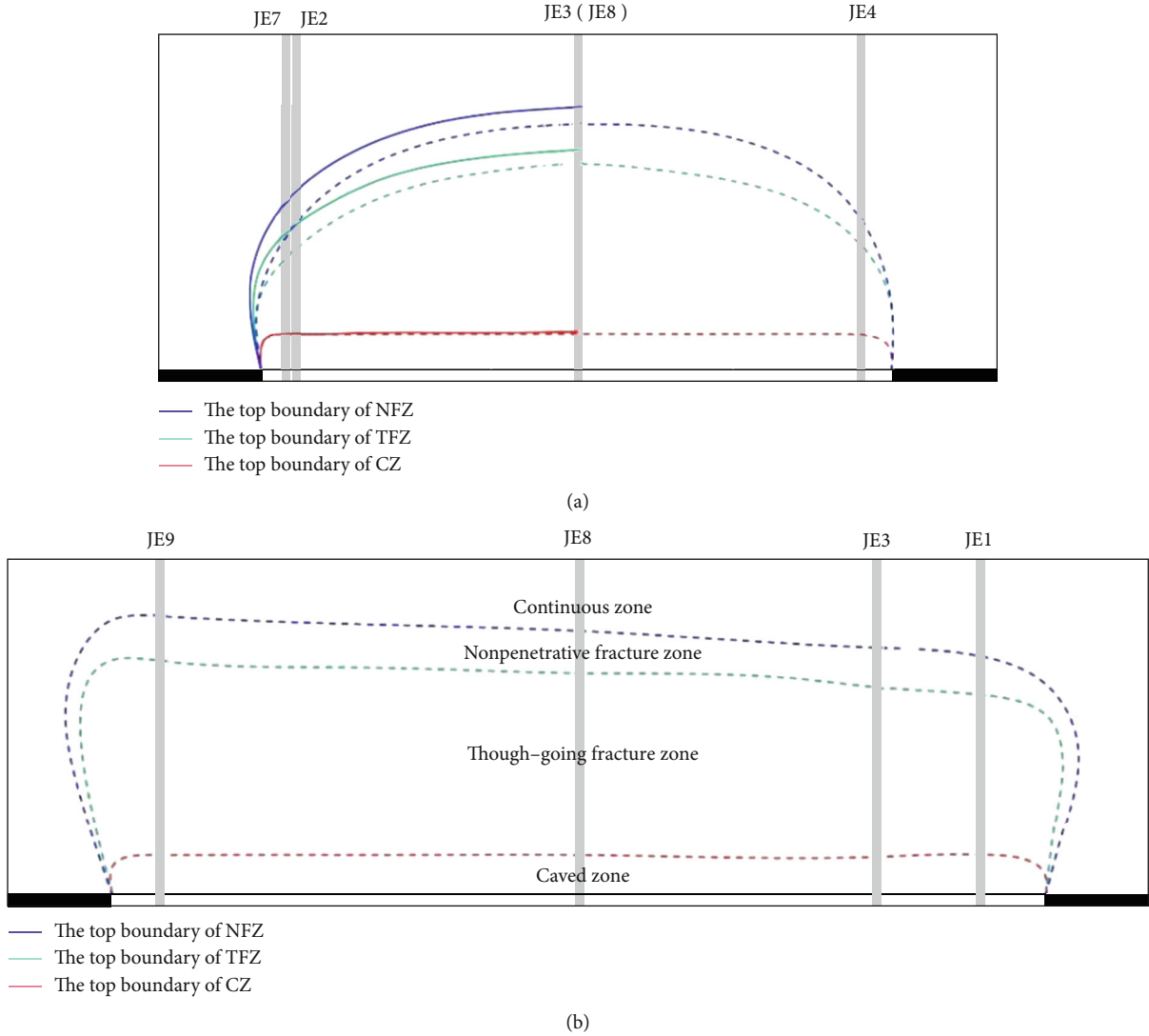
(a)

(b)

FIGURE 8: Profiles of top boundaries of CZ, TFZ, and NFZ.

TABLE 5: Top boundary depths and heights of the NFZ in boreholes.

Boreholes	Top boundary depths of the NFZ (m)					Heights of the NFZ (m)				
	DCA	DFLM	VCO	FPT	Results	DCA	DFLM	VCO	FPT	Results
JE1	143.93	143.73	143.79	143.7	143.7	18.00	18.20	18.14	18.23	18.23
JE2	—	187.99	—	187.96	187.96	—	11.52	—	11.55	11.55
JE3	137.43	137.41	137.45	137.42	137.41	18.80	18.82	18.78	18.81	18.82
JE4	182.04	182.1	182.04	182.31	182.04	12.09	12.03	12.09	11.82	12.09
JE5	—	—	—	—	—	0	0	0	0	0
JE6	—	—	—	—	—	0	0	0	0	0
JE7	167.8	167.73	167.75	167.73	167.73	14.35	14.42	14.40	14.42	14.42
JE8	—	135.15	—	135.11	135.11	—	20.00	—	20.04	20.04
JE9	—	120.51	120.68	120.61	120.51	—	21.20	21.03	21.10	21.20

The increasing extent of rock permeability is related not only to the lithology of the rock but also to the location in the NFZ (the distance from the coal seam). The estimated rock permeability coefficient of the lower part of the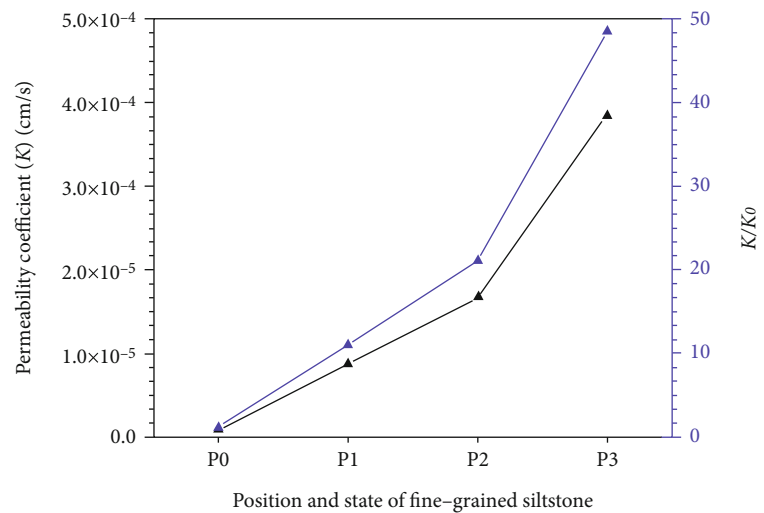 NFZ is an order of magnitude larger than that of the upper part. The permeability coefficients of rock in the upper, middle, and lower parts of the NFZ are approximately 10 times, 20 times, and 40 times, respectively, higher than those estimated for their premining rock samples.
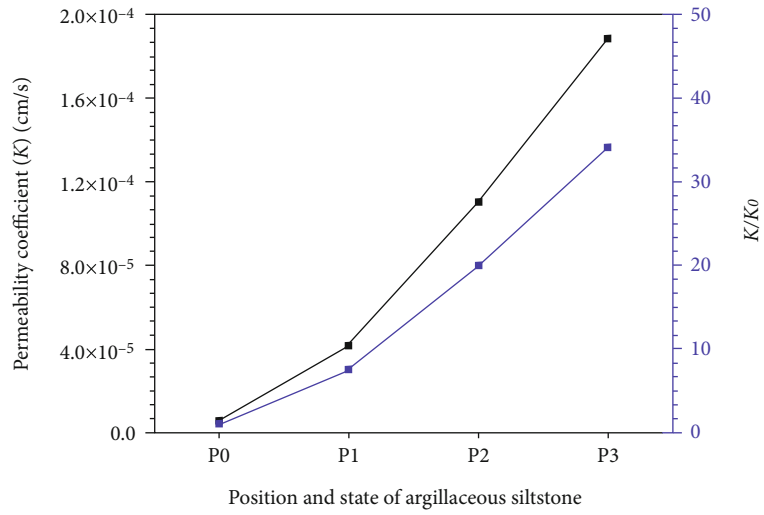
(a)
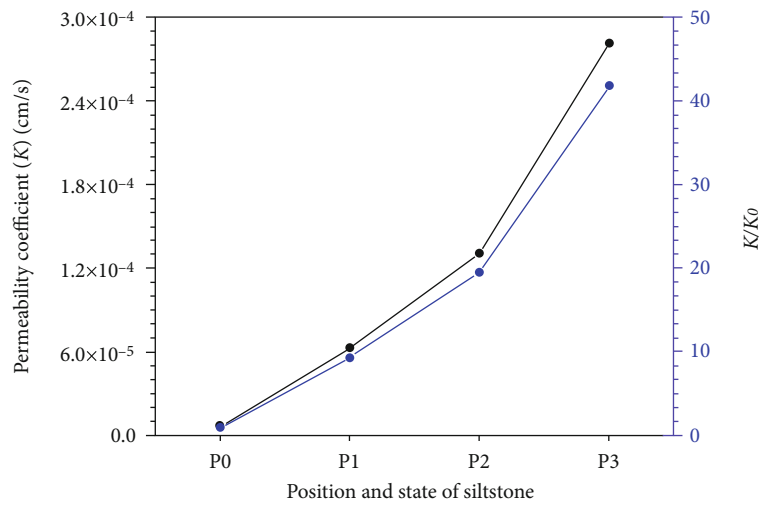
(b)

(c)

Figure 9: Permeability increase curves of rock with nonpenetrative fracture affected by coal mining: (a) argillaceous sandstone; (b) siltstone; (c) fine-grained sandstone.

6. Conclusions

According to the characteristics of fracture distribution and its potential effect on the leakage of sand phreatic water, the overlying strata was divided into four zones: CZ, TFZ, NFZ, and COZ, from the bottom to the top. The developmental height of CZ is relatively stable, which is roughly 4.36 times of the thickness of the mining coal seam. Along the advancing direction of the working face, the height of TFZ gradually increases to the maximum value of 93.09 m, approximately 16.93 times of the mining thickness. In the advancing direction, the vertical profile of TFZ was arch-shaped. The height of the NFZ ranges from 11.55 to 21.20 m, which is approximately 0.17 times of the combined height of CZ and TFZ. Affected by coal mining, the permeability of the rock in NFZ was increased by 7.52 to 48.37 times, and the magnitude of the increase is nonlinear from top to bottom. The results of the study are helpful to predict the potential loss of phreatic water and determine the mining thickness. It can provide the basis for water preserved mining in the arid and semiarid mining areas in western China.

Data Availability

The data used to support the findings of this study are included within the article.

Conflicts of Interest

The authors declare no conflict of interest.

Authors' Contributions

Yu Liu, Qimeng Liu, and Wenping Li designed and wrote the paper, Yu Liu and Qimeng Liu performed the experiments, and Youbiao Hu supervised the paper writing.

Acknowledgments

References

[1] P. Ameli, J. E. Elkhoury, J. P. Morris, and R. L. Detwiler, "Fracture permeability alteration due to chemical and mechanical processes: a coupled high-resolution model," *Rock Mechanics and Rock Engineering*, vol. 47, no. 5, pp. 1563–1573, 2014.

[2] S.-Y. Hamm, M. S. Kim, J.-Y. Cheong, J.-Y. Kim, M. Son, and T.-W. Kim, "Relationship between hydraulic conductivity and fracture properties estimated from packer tests and borehole data in a fractured granite," *Engineering Geology*, vol. 92, no. 1-2, pp. 73–87, 2007.

[3] Q.-x. Huang and W.-z. Zhang, "Research on downward crack closing of clay aquiclude in shallow coal seam safety mining,"

[4] China's National Bureau of Statistics, *China National Bureau of Statistics Statistical yearbook of china*, China Statistics Press, Beijing, 2019.

[5] Z. Bian, X. Miao, S. Lei, S.-e. Chen, W. Wang, and S. Struthers, "The challenges of reusing mining and mineral-processing wastes," *Science*, vol. 337, no. 6095, pp. 702-703, 2012.

[6] J. Wei, F. Wu, H. Yin et al., "Formation and height of the interconnected fractures zone after extraction of thick coal seams with weak overburden in western China," *Mine Water and the Environment*, vol. 36, no. 1, pp. 59–66, 2017.

[7] Z. H. Li, M. X. Ma, and Y. S. Bao, "Development and application of fluid-solid coupling similar materials in discharge test of old goaf water," *Geofluids*, vol. 2020, Article ID 8834885, 2020.

[8] B. A. Poulsen, "Coal pillar load calculation by pressure arch theory and near field extraction ratio," *International Journal of Rock Mechanics and Mining Sciences*, vol. 47, no. 7, pp. 1158–1165, 2010.

[9] X. X. Miao, X. Cui, J. Wang, and J. Xu, "The height of fractured water-conducting zone in undermined rock strata," *Engineering Geology*, vol. 120, no. 1-4, pp. 32–39, 2011.

[10] G. Wang, M. Wu, R. Wang, H. Xu, and X. Song, "Height of the mining-induced fractured zone above a coal face," *Engineering Geology*, vol. 216, pp. 140–152, 2017.

[11] G. R. Feng, J. Zheng, Y. F. Ren, C. M. Zhong, and L. X. Kang, "Mechanical model and analysis on movement of rock strata between coal seams in pillar upward mining of left-over coal," *Applied Mechanics and Materials*, vol. 58-60, pp. 393–398, 2011.

[12] T. Q. Liu, *Coal Mine Surface Movement, Overburden Failure and its Application*, China Coal Industry Publishing House, Beijing, 1981.

[13] L. Holla, "Ground movement due to longwall mining in high relief areas in new south wales, Australia," *International Journal of Rock Mechanics and Mining Sciences*, vol. 34, no. 5, pp. 775–787, 1997.

[14] V. Palchik, "Formation of fractured zones in overburden due to longwall mining," *Environmental Geology*, vol. 44, no. 1, pp. 28–38, 2003.

[15] S. Peng, *Surface Subsidence Engineering*, SME, New York, 1992.

[16] W. Q. Zhang, Z. Y. Wang, X. X. Zhu, W. Li, B. Gao, and H. Yu, "A risk assessment of a water-sand inrush during coal mining under a loose aquifer based on a factor analysis and the fisher model," *Journal of Hydrologic Engineering*, vol. 25, no. 8, article 4020033, 2020.

[17] D. Zhang, G. Fan, Y. Liu, and L. Ma, "Field trials of aquifer protection in longwall mining of shallow coal seams in China," *International Journal of Rock Mechanics and Mining Sciences*, vol. 47, no. 6, pp. 908–914, 2010.

[18] W. H. Sui, Y. Hang, L. Ma et al., "Interactions of overburden failure zones due to multiple-seam mining using longwall caving," *Bulletin of Engineering Geology and the Environment*, vol. 74, no. 3, pp. 1019–1035, 2015.

[19] F. Wang, S. Tu, C. Zhang, Y. Zhang, and Q. Bai, "Evolution mechanism of water-flowing zones and control technology for longwall mining in shallow coal seams beneath gully topography," *Environmental Earth Sciences*, vol. 75, no. 19, article 1039, 2016.

[20] H. Zha, W. Q. Liu, and Q. H. Liu, "Physical simulation of the water-conducting fracture zone of weak roofs in shallow seam

Journal of Coal Science and Engineering, vol. 17, no. 3, pp. 349–354, 2011.

mining based on a self-designed hydromechanical coupling experiment system," *Geofluids*, vol. 2020, Article ID 2586349, 2020.

[21] G. W. Fan and D. S. Zhang, "Mechanisms of aquifer protection in underground coal mining," *Mine Water and the Environment*, vol. 34, no. 1, pp. 95–104, 2015.

[22] W. Winters and R. Capo, "Ground water flow parameterization of an appalachian coal mine complex," *Ground Water*, vol. 42, no. 5, pp. 700–710, 2004.

[23] J. Wang and H. Park, "Coal mining above a confined aquifer," *International Journal of Rock Mechanics and Mining Sciences*, vol. 40, no. 4, pp. 537–551, 2003.

[24] J. Zhang, "Investigations of water inrushes from aquifers under coal seams," *International Journal of Rock Mechanics and Mining Sciences*, vol. 42, no. 3, pp. 350–360, 2005.

[25] Y. Xu, L. Ma, and Y. Yu, "Water preservation and conservation above coal mines using an innovative approach: a case study," *Energies*, vol. 13, no. 11, p. 2818, 2020.

[26] J. Blachowski and S. Ellefmo, "Numerical modelling of rock mass deformation in sublevel caving mining system," *Acta Geodynamica et Geomaterialia*, vol. 9, no. 9, pp. 379–388, 2012.

[27] Y. Wang, X. Li, and B. Zhang, "Numerical modeling of variable fluid injection-rate modes on fracturing network evolution in naturally fractured formations," *Energies*, vol. 9, no. 6, p. 414, 2016.

[28] L. Ma, Z. Jin, J. Liang, H. Sun, D. Zhang, and P. Li, "Simulation of water resource loss in short-distance coal seams disturbed by repeated mining," *Environmental Earth Sciences*, vol. 74, no. 7, pp. 5653–5662, 2015.

[29] D. Adhikary and H. Guo, "Modelling of longwall mining-induced strata permeability change," *Rock Mechanics and Rock Engineering*, vol. 48, no. 1, pp. 345–359, 2015.

[30] State Administration for Safety Management and Control of China, *Specification for building, water body, railroad and main mine lane coal pillar with pressure mining*, China Coal Industry Publishing House, Beijing, 2017.

[31] S. Liu, S. Dai, W. Li, B. Han, B. He, and J. Luo, "A new monitoring method for overlying strata failure height in Neogene laterite caused by underground coal mining," *Engineering Failure Analysis*, vol. 117, article 104796, 2020.

[32] Z. Meng, X. Shi, and G. Li, "Deformation, failure and permeability of coal-bearing strata during longwall mining," *Engineering Geology*, vol. 208, pp. 69–80, 2016.

[33] M. Li, J. Zhang, W. Zhang, A. Li, and W. Yin, "Experimental investigation of water-inrush risk based on permeability evolution in coal mine and backfill prevention discussion," *Goefluids*, vol. 2019, pp. 1–9, 2019.

[34] W. P. Li, Q. Q. Wang, and X. Q. Li, "Reconstruction of aquifuge: the engineering geological study of N2 laterite located in key aquifuge concerning coal mining with water protection in Northwest China," *Journal of Coal Science and Engineering*, vol. 42, no. 1, pp. 88–97, 2017, (In Chinese).

[35] S. L. Liu, W. P. Li, W. Qiao, X. Q. Li, Q. Q. Wang, and J. H. He, "Zoning for mining-induced environmental engineering geological patterns: a case study in the Yushenfu mining area, northern Shaanxi, China," *Journal of Hydrology*, vol. 579, article 124020, 2019.

[36] Y. Chen, S. Zhu, and S. Xiao, "Discussion on controlling factors of hydrogeochemistry and hydraulic connections of groundwater in different mining districts," *Natural Hazards*, vol. 99, no. 2, pp. 689–704, 2019.